Integrating Theoretical and Experimental Approaches to Unveil the Mechanical Properties of $CuSbSe_2$ Thin Films

Ozge Surucu[a*+], Aysenur Gencer[b], Gokhan Surucu[c], Demet Usanmaz[d], Mehmet Parlak[e,]

[a]*Department of Electrical and Electronics Engineering, Atilim University, 06836, Ankara, Türkiye*

[b]*Department of Physics, Karamanoglu Mehmetbey University, 70200, Karaman, Türkiye*

[c]*Department of Energy Systems Engineering, Gazi University, 06500, Ankara, Türkiye*

[d] *Department of Natural Sciences, Kettering University, Flint, MI 48504, USA*

[e]*Department of Physics, Middle East Technical University, 06800, Ankara, Türkiye*

Abstract

An exhaustive investigation of the mechanical characteristics of $CuSbSe_2$ thin films is conducted in this study by combining experimental nanoindentation methods with theoretical simulations. The Ab-initio Molecular Dynamics (AIMD) calculations are performed with the machine learning (ML) force fields. By employing the Vienna Ab-initio Simulation Package (VASP) based on Density Functional Theory (DFT), theoretical inquiries are carried out to identify crucial parameters, such as bonding characteristics, elastic constants, hardness, bulk modulus, shear modulus, Young's modulus, and Poisson's ratio. Experimental validation is conducted using nanoindentation to investigate load-dependent hardness and Young's modulus in a manner that closely matches the theorized predictions. The anomalies between experimental and theoretical outcomes are ascribed to anisotropic behavior and grain boundaries. Furthermore, an investigation is conducted into the directional dependence of sound wave velocities in the $CuSbSe_2$ films, leading to the revelation of intricate elastic property details. By employing an integrated theoretical-experimental approach, the present attempt not only increases the knowledge concerning $CuSbSe_2$ films but also fortifies the relationship between theory and experiment, thereby bolstering the dependability of our results. The insights provided as a result of this paper facilitate the development of $CuSbSe_2$ film applications in a variety of technological fields in the future.

[+] *published by Physica Scripta, http://dx.doi.org/10.1088/1402-4896/ad8f03, Department of Electrical and Electronics Engineering, Atilim University, 06836, Ankara, Türkiye*

Keywords: Nanoindentation; Density Functional Theory; Ab-initio Molecular Dynamics (AIMD); Machine-learning Force Fields (MLFF); Mechanical properties
**Email:* *ozge.surucu@atilim.edu.tr*

Introduction

For long, solar cells, capable of converting sunlight into electrical power, have been considered among the cleanest, most reliable, and most renewable energy sources to meet the future energy demands of the world [1,2]. Remarkable advancements in solar cell technology, particularly in increasing conversion efficiency and enhancing durability, have been reported over the past few decades [3,4]. The shift from bulk silicon to thin-film solar cells has significantly reduced manufacturing costs and opened up possibilities for lightweight and flexible designs. Notably, materials like Cadmium Telluride (CdTe), Copper Indium Gallium Selenide (CIGS), and perovskites have shown great promise [4]. However, despite the advantages in cost and efficiency, concerns regarding the scarcity and toxicity of these materials persist. Consequently, there is a growing interest in developing thin-film solar cells using earth-abundant substances to ensure sustainability and cost-effectiveness [5–9].

Among the promising earth-abundant thin-film materials, compounds such as copper zinc tin sulfide (CZTS), copper zinc tin selenide (CZTSe), and copper zinc tin sulpho-selenide (CZTSSe) have garnered significant attention for their high absorption coefficients, favorable optoelectronic properties, and low toxicity [10,11] [12]. Copper antimony selenide ($CuSbSe_2$) emerges as another promising candidate, offering superior thermal stability, higher absorption coefficients, and simpler synthesis compared to other materials [13][14][15][16]. Despite the abundance of research on the optical and electrical properties of $CuSbSe_2$, studies on its mechanical properties remain limited [17–19]. Recent studies have highlighted the importance of mechanical properties in the performance and durability of solar cells. The mechanical behavior is closely related to the thickness and Young's modulus of the thin films and substrates involved, which are critical in predicting strain distribution [20]. For example, Young's modulus values have been reported for materials like Mo and CIGS thin films, emphasizing the need for detailed mechanical characterization [21]. Given the mechanical stresses photovoltaic devices endure, such as temperature fluctuations and bending, understanding the mechanical strength and behavior of

$CuSbSe_2$ thin films becomes crucial. This is particularly important for ensuring the reliability and durability of photovoltaic absorbers under operational conditions [22,23][24,25]. Therefore, this research aims to address this gap by investigating the mechanical properties of $CuSbSe_2$ thin films, using a combination of DFT calculations and nanoindentation experiments. The key properties, including elastic constants, bulk modulus, and Poisson's ratio, under various conditions, are explored to provide insights into the material's potential as a durable photovoltaic absorber.

Materials and Methods

Theoretical Calculation Details

The theoretical investigations of the $CuSbSe_2$ thin film is performed using the Vienna Ab-initio Simulation Package (VASP) [26,27] based on Density Functional Theory (DFT). The electron-electron interactions are considered using the Perdew-Burke-Ernzerhof (PBE) functional [28] within the generalized gradient approximation (GGA). The electron-ion interactions are studied with the Projector Augmented Wave (PAW) method [29,30]. The cut-off energy for the wavefunctions are chosen as 600 eV with the energy and force convergences as 10^{-9} eV and 10^{-6} eV/Å, respectively. The **k**-point sampling is carried out using a gamma-centered scheme [31] with 4×2×1 **k**-points. The valence electron configurations are $3d^{10}4s^1$, $5s^25p^3$, and $4s^24p^4$ for the Cu, Sb, and Se atoms, respectively. The $CuSbSe_2$ thin films are considered for the AIMD calculations using a 3×2×1 supercell at zero pressure and 300 K temperature. For AIMD calculations, the dynamic variables are chosen as lattice parameters and atomic positions. The Langevin thermostat [32–34] is used with the atomic friction coefficients as 10 ps^{-1}, 12 ps^{-1}, and 8 ps^{-1} for Cu, Sb, and Se atoms respectively. Also, the lattice friction coefficient is taken as 12 ps^{-1}. The time step for the AIMD calculations are taken as 2 fs with Verlet algorithm to solve the equations of motion of ions. The machine-learned force fields (MLFF) [35,36] are implemented in VASP which enables to speed up the AIMD calculations. The MLFF is employed for the $CuSbSe_2$ thin film with using descriptors based on the Gaussian representation of atomic distributions [35,37]. The Bayesian linear regression [36] which enables to reliable estimations, is used to obtain the energies, forces and stress components. The Bader partial charges are determined using VASP and analyzed using the Bader partial charge program developed by Henkelman group [38] which is based on a suggestion by Bader [39]. The optimized structure obtained from the VASP program is employed in the VESTA program [40] to obtain the X ray diffraction (XRD) pattern for the $CuSbSe_2$ thin

film with a Cu Kα source which has a wavelength of 1.541 Å. The elastic constants for the $CuSbSe_2$ thin film is obtained using the stress-strain method implemented in VASP [41]. The hardness is obtained using the method given in [42]. The directional dependence of the elastic properties are visualized in 2D and 3D using the ELATE program [43]. Furthermore, the sound wave velocities are obtained using the Christoffel tool [44], which uses the elastic stiffness matrix to solve the Christoffel equation [45].

Experimental Details

$CuSbSe_2$ thin films are produced by co-evaporation technique using CuSe and Sb_2Se_3 (commercially purchased) sources. The ambient pressure hovers around 10^{-5} Torr during deposition according to the results obtained in the optimization studies in this paper, along with the $CuSbSe_2$ thin film phase diagram provided by Welch et al. [46]. During deposition, the substrate temperature is initially maintained at room temperature and then, gradually increased to 300 ºC. After this temperature rise, the deposition is continued under Sb_2Se_3 steam. This process has been optimized based on our previous studies, which demonstrate that maintaining the substrate temperature within this range enhances the crystalline quality and electrical properties of the films [47,48]. The Cu-Sb-Se phase diagram further supports this approach as critical for achieving the desired phase formation and stoichiometry essential for high-efficiency solar cell performance. The XRD measurements are performed with a Rigaku Miniflex diffractometer with Cu Kα radiation to examine the crystal structure of the obtained films. The obtained XRD pattern is presented in Figure 2. As expected, it is observed that a crystalline structure is formed on the films. The nanoindentation measurements are performed to examine the mechanical properties of the films. To do this, a Diamond Berkovich tip CSM device is used. The nanoindentation measurements are performed using a Berkovich diamond indenter (Serial number: B-J 90) on the NHTTX instrument (S/N: 01-03089). The indentation process is conducted with a maximum load of 5.00 mN, a loading rate of 10.00 mN/min, and an acquisition rate of 10.0 Hz. The unloading rate is maintained at 10.00 mN/min, with a 5-second pause at maximum load.

For calibration, the system is first calibrated using a reference material with known mechanical properties to ensure the accuracy of the depth and force measurements. This process involves adjusting the instrument's sensor settings, including the Delta Slope Contact, which is set at 90%, to minimize the effects of thermal drift and tip wear. Additionally, an error analysis is performed

by conducting multiple indentation tests on the reference material. The results are used to calculate the standard deviation and standard error, which provides a quantifiable measure of the uncertainty in the reported mechanical properties.

Results and Discussions

Figure 1 represents the structural properties of the $CuSbSe_2$ thin film as investigated in the stable orthorhombic crystal structure with space group Pnma (#62). The optimized lattice parameters a=6.46 Å, b=4.04 Å, and c=15.01 Å agree with the previously reported results (a=6.38 Å, b=4.00 Å, and c=15.11 Å [49], a=6.2988 Å, b=3.981 Å, and c=15.003 Å [50]) . The bond lengths between Cu--Se and Se--Sb are 2.43 and 3.21 Å, respectively, and these values are also consistent with literature reports [51,52]. The thermal stability of the $CuSbSe_2$ thin film at 300 K are investigated through the evaluation of ab initio molecular dynamics (AIMD) trajectories with the implementation of the machine learning force fields (MLFF) in VASP. In this respect, the force fields are generated on the fly during the AIMD calculations and the Bayesian errors are predicted at each step to decide whether a first-principles calculation is performed or not. Therefore, the AIMD with MLFF simulations are performed to accelerate the MD simulations. Figure 2 illustrates the AIMD simulations of the $CuSbSe_2$ thin film at a temperature of 300 K. An examination of the AIMD trajectories demonstrates that the structure remained undamaged at 300 K with extremely stable energy and temperature. This finding will definitely stimulate efforts in experimental synthesis of $CuSbSe_2$ thin films. The calculated X-ray diffraction pattern and Miller indices given on the peaks are presented in Figure 3, showing a good match with the experimental results. The maximum peak is at the (0 1 3) direction for the $CuSbSe_2$ thin film.

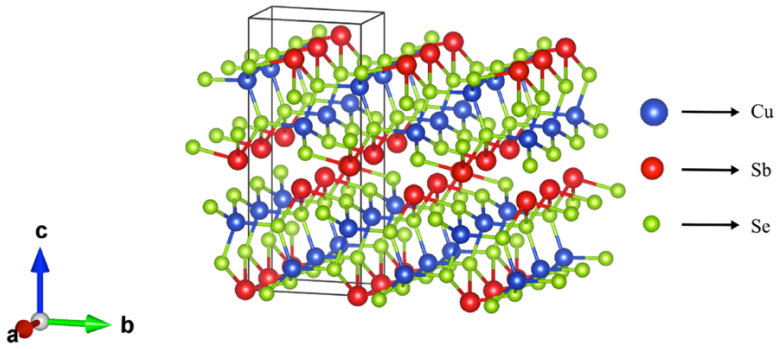

Figure 1: The crystal structure of the $CuSbSe_2$ thin film

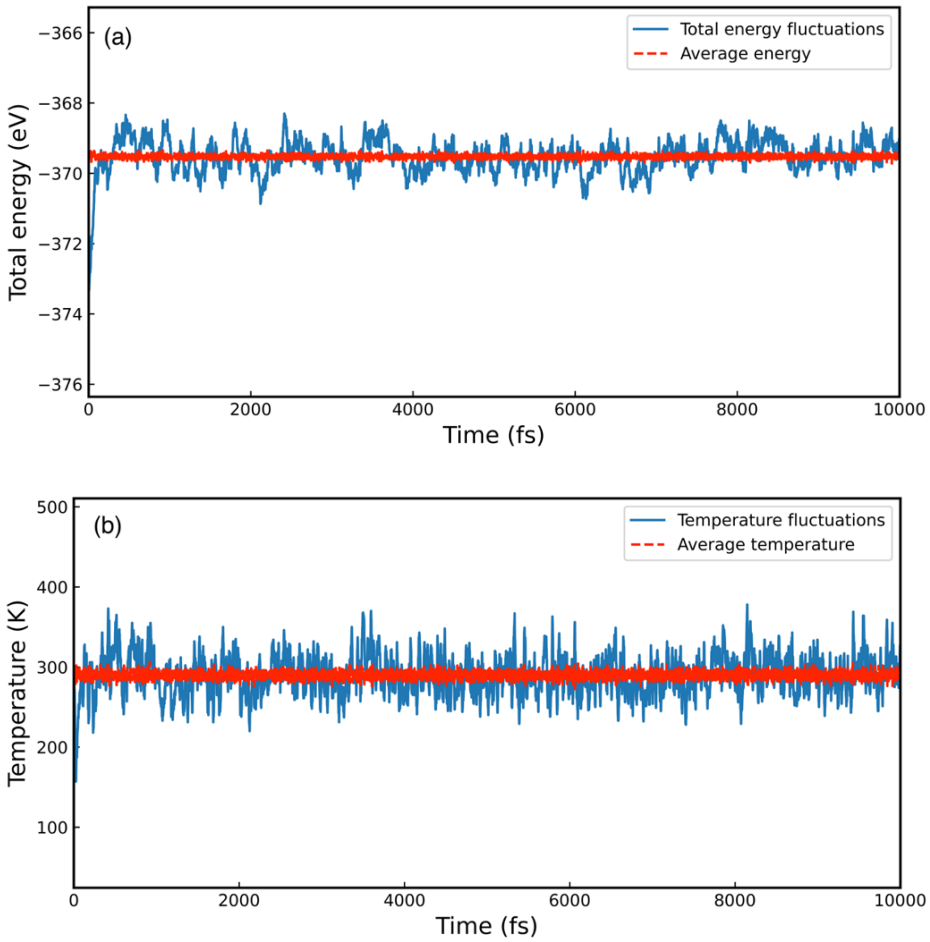

Figure 2: (a) Total energy and (b) temperature for the $CuSbSe_2$ thin film as a function of time during AIMD calculations. The blue curves show the total energy fluctuation and the temperature fluctuation while the red ones show the average total energy and average temperature.

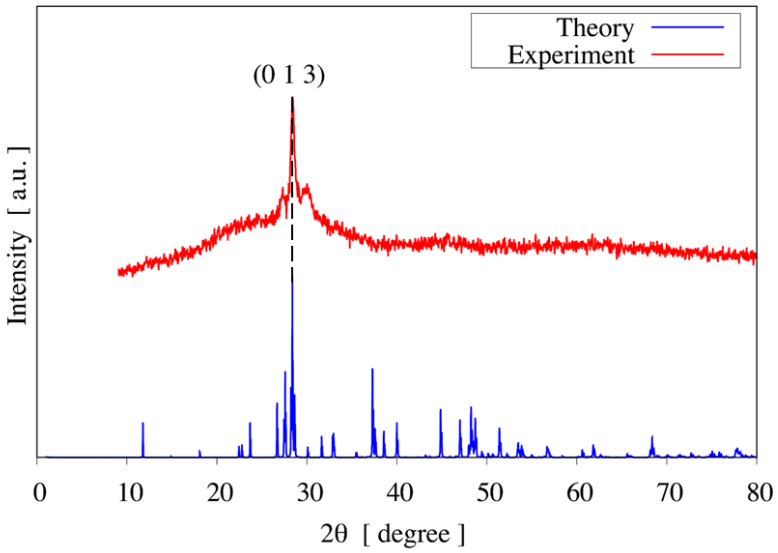

Figure 3: The X-ray diffraction pattern for the $CuSbSe_2$ thin film. The red and blue curves show the experimental and theoretical results, respectively.

Examining the mechanical properties of materials is essential for technological applications, enabling the obtaining of anisotropic elastic properties. For this purpose, the elastic constants for the $CuSbSe_2$ thin film are calculated by the stress-strain method using VASP. Table 1 lists these constants, which amount to eight due to the orthorhombic crystal structure. The calculated constants satisfy the Born stability criteria [53] given in Equation 1, indicating the mechanical stability of the $CuSbSe_2$ thin film.

$$C_{11} > 0$$
$$C_{11}C_{22} > C_{12}^2$$
$$C_{11}C_{22}C_{33} + 2C_{12}C_{13}C_{23} - C_{11}C_{23}^2 - C_{22}C_{13}^2 - C_{33}C_{12}^2 > 0 \quad (1)$$
$$C_{44} > 0, C_{55} > 0, C_{66} > 0$$

Table 1: Elastic constants (C_{ij} – GPa), bulk modulus (B – GPa), shear modulus (G – GPa), Young's modulus (E – GPa), Poisson's ratio (ν), G/B, ratio, B/G ratio,, hardness (H – GPa), average mass per atom (M_a – 10^{-26} kg/mol), density of number of atoms per volume (n – 10^{28}), density (ρ – $g.cm^{-3}$), minimum thermal conductivity obtained with Clarke and Cahill models (λ_{Clarke} and λ_{Cahill} – W. $m^{-1}.K^{-1}$) for $CuSbSe_2$ thin film

C_{11}	**C_{12}**	**C_{13}**	**C_{22}**	**C_{33}**
97.30	35.00	53.93	97.45	95.37
C_{44}	**C_{55}**	**C_{66}**	**B**	**G**
26.18	30.78	28.23	61.14	27.32
E	**ν**	**G/B**	**B/G**	**H**
71.34	0.31	0.45	2.24	3.92
M_a	**n**	**ρ**	**λ_{Clarke}**	**λ_{Cahill}**
14.25	4.00	5.82	0.50	0.56

The bulk modulus (B, measure of the volume change under a hydrostatically applied pressure), shear modulus (G, the measure of the deformation as a result of shear stress applied to a surface), Young's modulus (E, the ratio of the stress to the strain), Poisson's ratio (ν), and the G/B and B/G ratios of this thin film are calculated using the obtained elastic constants, and the results are consistent with the reported study [54]. Among the listed moduli in Table 1**,** Young's modulus is the highest, which implies that the $CuSbSe_2$ thin film is more resistant to stress. A measure of contraction or expansion in other directions of the material when tension or compression is applied, the Poisson's ratio is used to identify the dominant bonding type in the compound. The Poisson's ratio around 0.25 (0.10) indicates that the compound has dominantly ionic (covalent) bonding [55]. The G/B ratio, which is around 0.60 (1.10), is also used to determine the bonding type of a material as a dominantly ionic (covalent) bond [55]. According to Table 1, $CuSbSe_2$ thin film has dominantly ionic bonding. Furthermore, the electron density distribution is obtained for the $CuSbSe_2$ thin film for the (1 0 0) plane and is shown in Figure 4. According to this figure, the ionic bonding is the dominantly bonding type for the $CuSbSe_2$ thin film. In addition to the bonding type, the Bader charges are obtained for the $CuSbSe_2$ thin film where the Cu, Sb and Se atoms have -1.14 e, 2.72 e, and -1.58 e Bader net partial charges, respectively where the total Bader charge is

zero. The charge is transferred away from the Sb atoms due having positive Bader partial charge while it is transferred to the Cu and Se atoms due having negative Bader partial charges [56]. In case of the $CuSbSe_2$ thin film, the B/G ratio stands greater than 1.75, hence classifying it as brittle. Moreover, as listed in Table 1, the hardness for the $CuSbSe_2$ thin film is obtained as 3.92 GPa, which is consistent with the nanoindentation results presented in the next section. In addition to these mechanical characteristics, Table 1 lists the minimum thermal conductivity (λ) of $CuSbSe_2$ thin film obtained from the Clarke [57] and Cahill [58] models. For these models, average mass per atom (M_a), density of the number of atoms per volume (n), and density of the material (ρ) are required, and they are listed in Table 1. The minimum thermal conductivities determined using the Clarke and Cahill models are 0.50 $W.m^{-1}.K^{-1}$ and 0.56 $W.m^{-1}.K^{-1}$ for $CuSbSe_2$ thin film, respectively. These thermal conductivities are low, which reveals the potential of this material for solar cell applications.

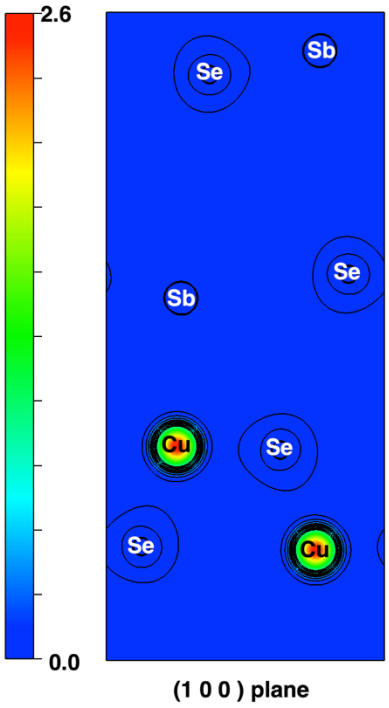

Figure 4: Electron density distribution of the $CuSbSe_2$ thin film for (1 0 0) plane

Figure 5 presents the anisotropic elastic properties [59] that are crucial to provide information related to the microcracks, dislocations, plastic deformations, etc., of $CuSbSe_2$ thin film in 2D and 3D obtained with the ELATE software [43]. The distorted shapes in Figure 4 indicate anisotropy.

It can be seen that the anisotropy for Young's modulus is higher in the *y* and *z* directions than in the *x* direction. Furthermore, the linear compressibility of the film has higher anisotropy in the *x* and *y* directions than in *z*, while the shear modulus has similar anisotropy in all directions. The Poisson's ratio has higher anisotropy in the *x* and *z* directions than in the *y* direction.

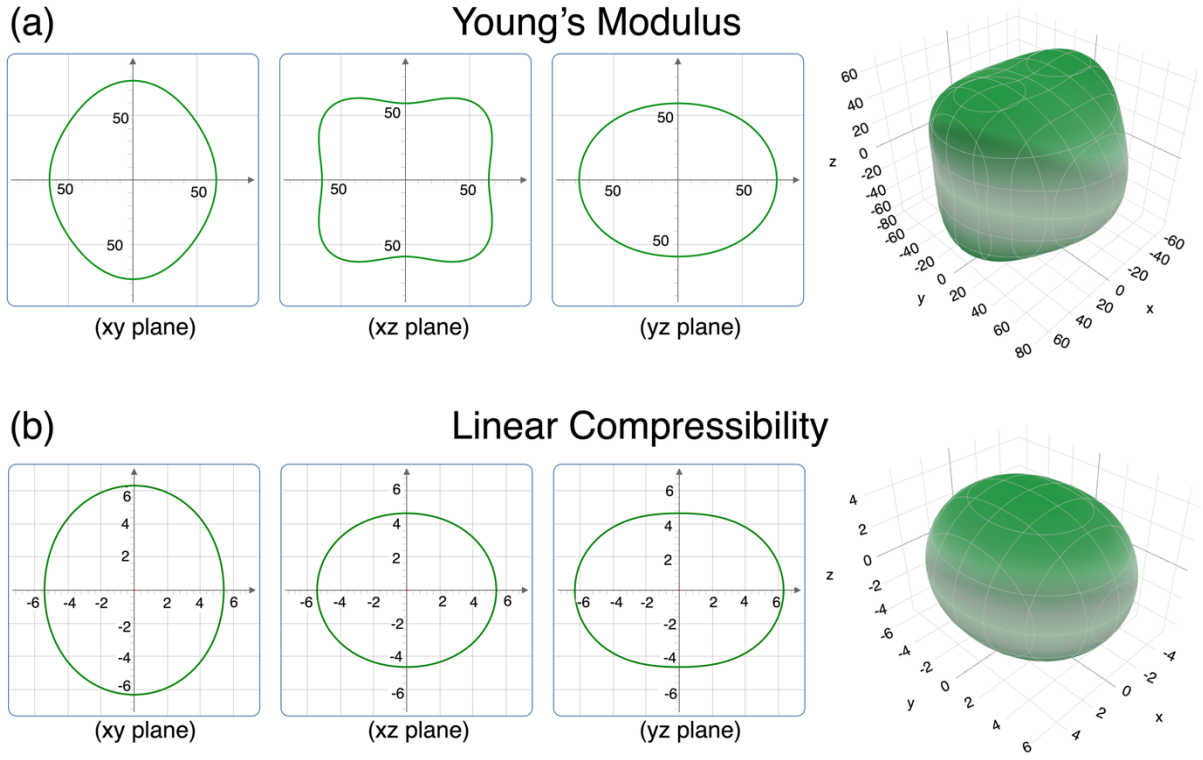

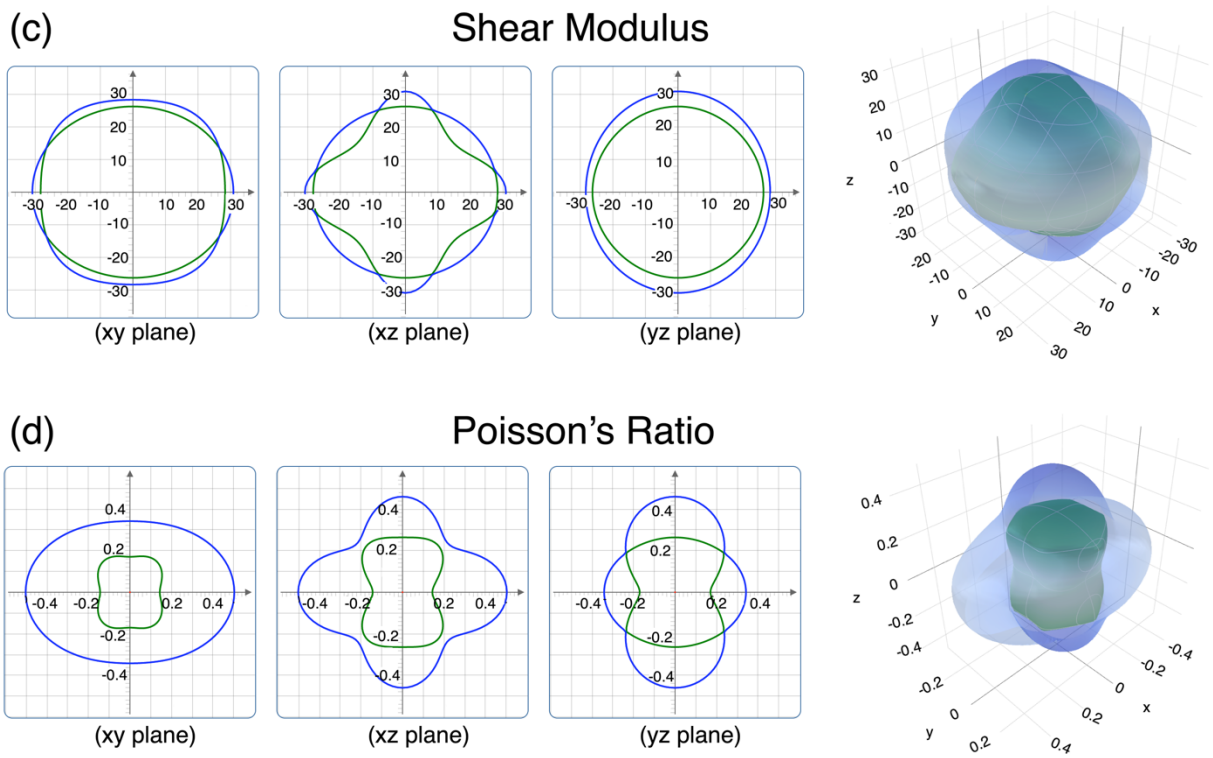

Figure 5: 2D and 3D representation for (a) Young's modulus, (b) linear compressibility, (c) shear modulus, and (d) Poisson's ratio of the $CuSbSe_2$ thin film

The calculation of sound wave velocities can provide valuable insights into the mechanical behavior of a material. Sound wave velocity refers to the speed of sound waves traveling through a solid material, and it is influenced by characteristics such as density, elastic modulus, and Poisson's ratio. Concerning $CuSbSe_2$ thin film, one can use such analysis in order to shed light on stiffness, strength, and ductility; high velocities are indicative of high stiffness and strength, while low velocities suggest greater ductility and deformability. Sound wave velocity analysis, in this way, can aid in the design and optimization of photovoltaic devices using $CuSbSe_2$ thin film with improved mechanical properties.

The sound wave velocities for the $CuSbSe_2$ thin film are obtained using the Christoffel tool, which employs an elastic stiffness matrix to perform the procedure. Figure 6 shows the group wave velocity, phase wave velocity, phase polarization, enhancement factor, and power flow sphere for the $CuSbSe_2$ thin film. Accordingly, the sound wave velocities are grouped into two transverse wave velocities along two directions and longitudinal wave velocities shown as slow secondary,

fast secondary, and primary modes, respectively. Figure 6a and Figure 6b show the group wave velocity and phase wave velocity with maximum values along the *x, y,* and *z* directions for slow secondary and fast secondary modes and minimum values along these directions for the primary mode. As seen in Figure 6c, the enhancement factor, which is calculated as the ratio of the group wave velocity to the phase wave velocity, has lower values in the *x, y,* and *z* directions in the primary and slow secondary modes and higher values in these directions for the fast secondary mode. The angle formed by the group wave velocity and the phase velocity is known as the 'power flow angle', depicted in Figure 6d as having low values in the *x, y,* and *z* directions for both secondary and primary modes.

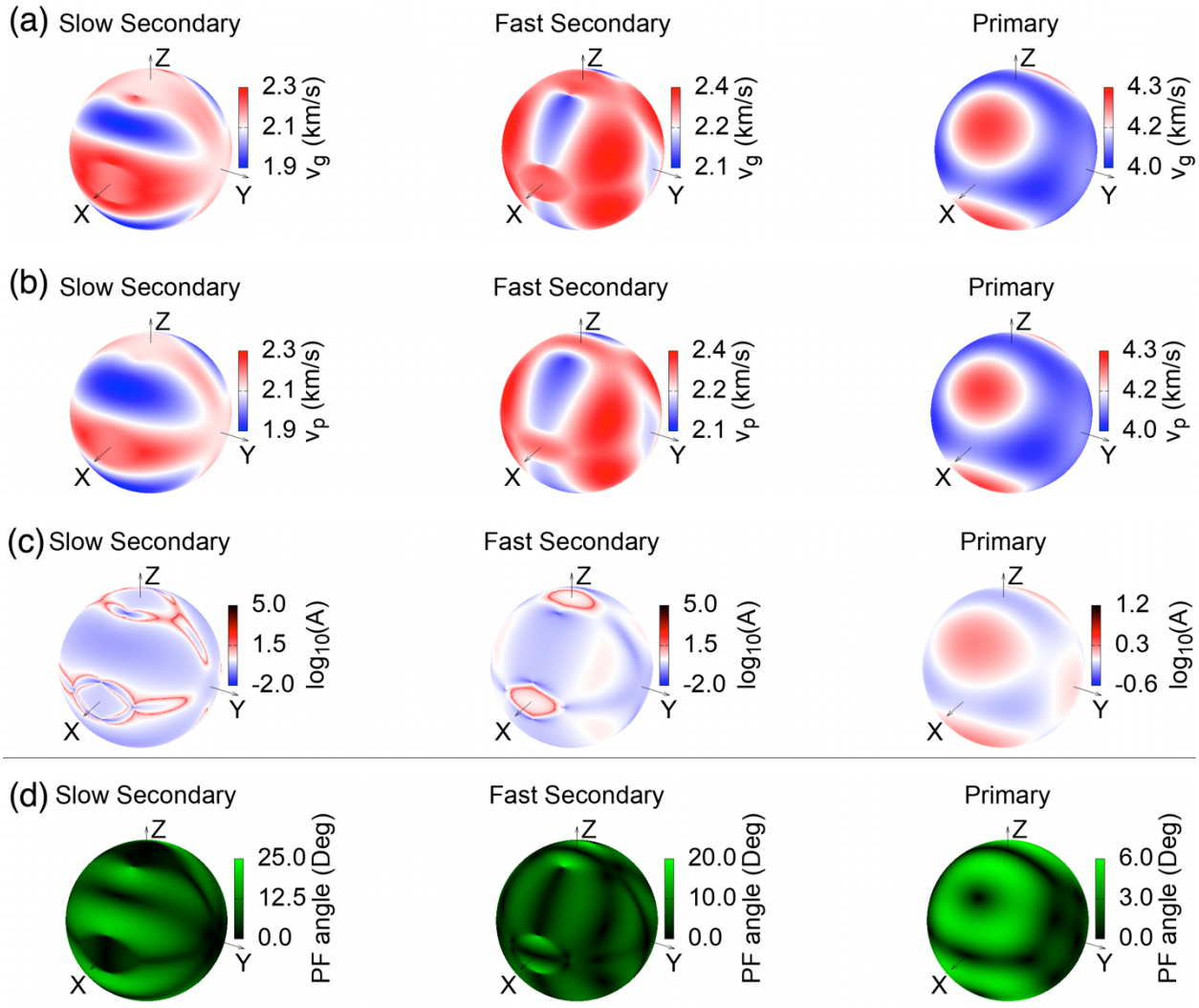

Figure 6: Direction dependence of (a) group velocity, (b) phase velocity, (c) enhancement factor, and (d) power flow angle for slow secondary, fast secondary, and primary modes of the $CuSbSe_2$ thin film

Understanding the mechanical properties of $CuSbSe_2$ thin films requires linking the theoretical insights gained from Density Functional Theory (DFT) simulations with the experimental results obtained through nanoindentation measurements. The nanoindentation measurements perform a critical role in validating theoretical predictions. Through nanoindentation, the mechanical properties of the material are carefully probed, and its nanoscale hardness, elasticity, and deformation behavior are analyzed. The accuracy of the computational models is validated by correlating theoretical predictions with experimental outcomes, thereby establishing a strong connection between theory and experimentation. This synergy between theoretical and experimental approaches not only increases the reliability of the findings here, but also provides a thorough understanding of the mechanical behavior of the $CuSbSe_2$ thin films. Apart from this, the combination of these methodologies allows for a nuanced investigation of the mechanical properties of the material, bridging the gap between theoretical predictions and real-world observations and significantly contributing to the advancement of knowledge in this field.

The hardness and Young's Modulus of the $CuSbSe_2$ thin film are determined by nanoindentation experiments at different loads between 0.25 and 5 mN and applied to the crystal surface. Graphs of the measured load (F) and penetration depth (h) are shown in Figure 7. Each graph shows the loading (plastic) and unloading (elastic) zones.The hardness (H) and Young's modulus (E) for the $CuSbSe_2$ thin film are obtained from the software included in the tester experiment. Briefly, the calculations made by the software are as follows:

Hardness is related to the cutter maximum load (F_{max}) and the projected contact area (A) [60] as:

$$H = \frac{F_{max}}{A} \qquad (2)$$

For the perfect Berkovich recess $A = 24.56h_c^2$,the actual contact depth (h_C) is determined from the first part of the discharge curve. The slope (dF/dh) of this part and the point of intersection of the linearly placed line on the indentation depth axis are equal to the stiffness (S) and h_c, respectively. The Oliver-Pharr analyses offer the following statements [61]:

$$S = 2\beta E_r \sqrt{\frac{A}{\pi}} \qquad (3)$$

$$\frac{1}{E_r} = \frac{1-v_f^2}{E} + \frac{1-v_i^2}{E_i} \qquad (4)$$

E_r = 1141 GPa in Eq. 3 and Eq 4 and is the elastic modulus of the diamond used as the tip in indentation. β= 1.034 for the Berkovich indentation, and the Poisson's ratios for the crystal and indentation used are v_f= 0.31 and v_i= 0.07, respectively.

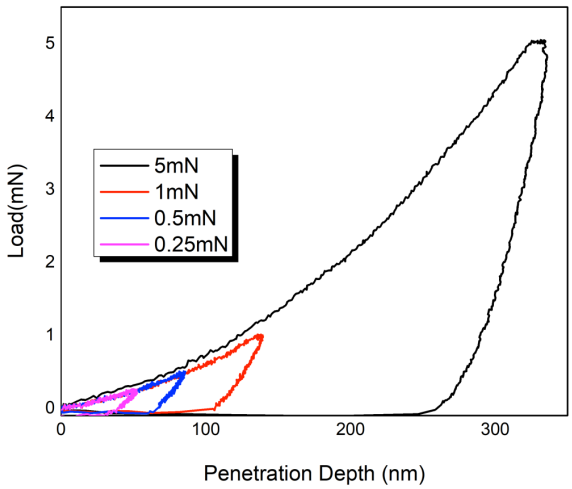

Figure 7: Penetration depth graphs for the $CuSbSe_2$ thin film against loads between 0.25 mN and 5 mN

The load-dependent hardness graph is shown in Figure 8. As can be seen from the figure, the hardness decreases as the load increases.

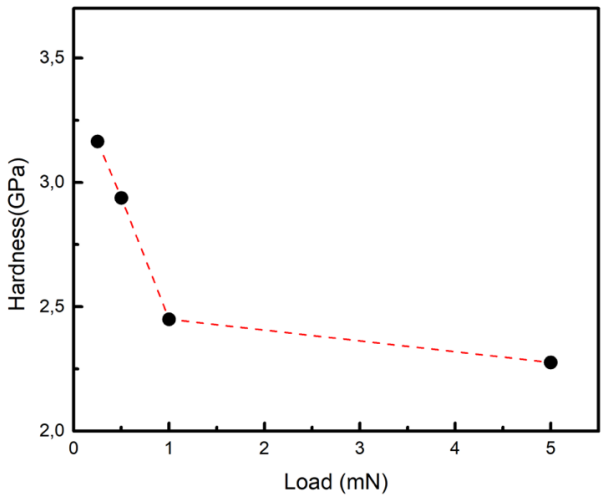

Figure 8: Load-dependent graph of nanoindentation hardness

The mean hardness of the $CuSbSe_2$ thin film was found to be 2.73 GPa, with a standard deviation of 0.33 GPa and a standard error of 0.17 GPa across different loads. The actual hardness value of the compound can be determined from the proportional specimen resistance (PSR) model, which was previously applied to other materials, such as Ho^{3+}:BaY_2F_8 [17], Sn [18], $AlMgB_{14}$ [64] and $LiTaO_3$ [20]. In this model, F_{max} and h_c are restated as follows:

$$\frac{F_{max}}{h_c} = \delta_1 + \delta_2 h_c \quad (5)$$

Here δ_1 and δ_2 are constants determined from the linear fit analyses of the graph F_{max}/ h_c dependent on h_c, shown in Figure 9. Using the slope and intersection point of the line on the vertical axis, these constants are found to be δ_1= 0.0032 mN/nm and δ_2= 4.48 × 10^{-5} mN/nm^2.

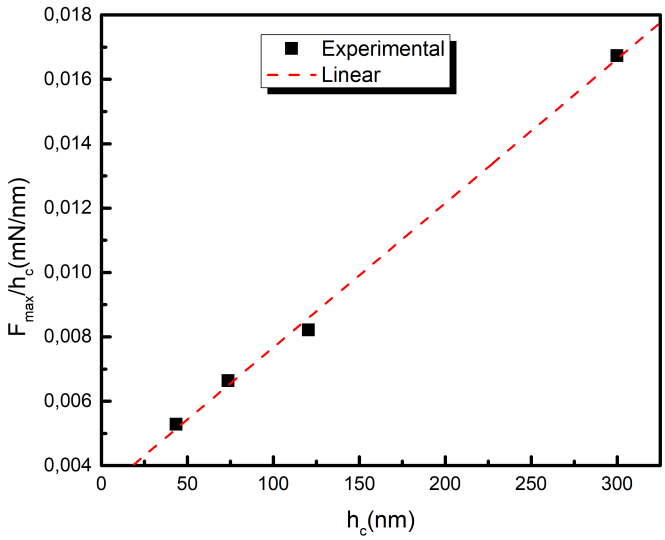

Figure 9: F_{max}/h_c plot based on h_c. The dashed line shows the linear fit.

The ln(h_c) versus ln(F_{max}) plot is shown in Figure 10, and it can help to determine whether this material exhibits ISE (Intendation Size Effect) behavior at the slope of this graph. The ISE behavior is also illustrated by Meyer's [66] law, which states:

$$F_{max} = Ah_c^n \ (6)$$

where A is a constant and n symbolizes the Meyer index. The load-independent stiffness behavior is observed at n = 2, with n < 2 indicating the presence of ISE behavior. From the slope of the graph in Figure 10, the value of n is obtained as 0.63. This value shows that $CuSbSe_2$ thin film has ISE behavior.

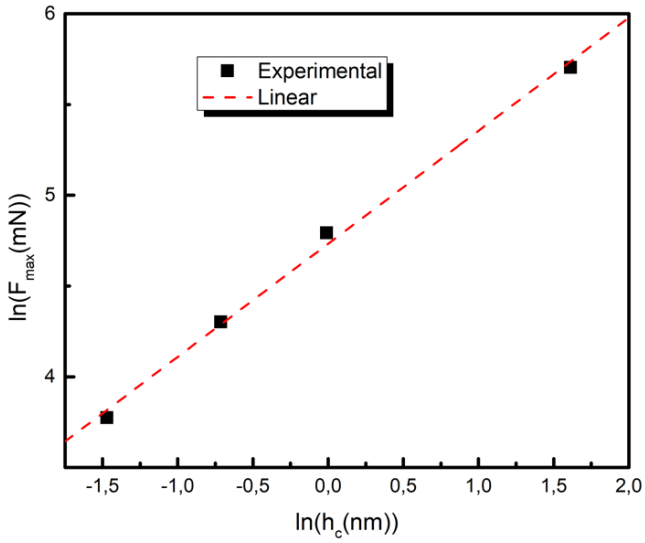

Figure 10: The ln(hc) versus ln(Fmax/hc) plot. The dashed line shows the linear fit.

The Young's modulus of $CuSbSe_2$ thin film is found using Eq. (3). Table 2 lists the load-dependent Young's modulus values. The theoretical Modulus of Young listed in Table 1 is 71.34 GPa, and the experimental Modulus values in Table 2 are close to this value. The difference is due to the DFT calculations and experimental measurements, and the reasons for this difference are attributed to the following factors [67–69]: (i) The DFT calculations were performed on a theoretically perfect crystal structure. (ii) For $CuSbSe_2$ thin film, it may contain grain boundaries that affect experimental nanoindentation measurements. In this attempt, the grain boundaries were ignored in DFT calculations. (iii) The anisotropic behavior of $CuSbSe_2$ thin film can lead to significant differences between the calculated and experimentally determined values. (iv) Excessive binding issues, binding energy, and bond length differences considered in the theoretical calculations and nanoindentation experiments may have affected the results of the proceeding analyses.

Table 2: Load-dependent Young's modulus values for $CuSbSe_2$ thin film

Load (mN)	Young modulus (GPa)
0.25	66.690
0.50	66.852
1.00	52.627

5.00	61.955

Conclusion

The present research examines in detail the mechanical characteristics of $CuSbSe_2$ thin films by means of integrating experimental nanoindentation methods and theoretical calculations. The theoretical investigations are carried out utilizing the Vienna Ab-initio Simulation Package (VASP), and the machine-learning force fields (MLFF) is employed to obtain the ab-initio molecular dynamics (AIMD) calculations at 300K. The AIMD results show that $CuSbSe_2$ thin film has small fluctuations in total energy and temperature that reveal the thermal equilibrium. Density Functional Theory (DFT) yields significant findings pertaining to the bonding properties, hardness, bulk modulus, shear modulus, Young's modulus, and Poisson's ratio of $CuSbSe_2$ thin films. Our results reveal that ionic bonding dominates – a finding which is confirmed by the Poisson's ratio and G/B ratio calculations. The brittle characteristics of the material are further corroborated by the experimental hardness value of 3.92 GPa, as indicated by the calculated B/G ratio.

The results obtained from the experimental validation of nanoindentation measurements substantiate our theoretical forecasts. The load-dependent hardness and Young's modulus values observed in the nanoindentation experiments are found to be in close agreement with the theoretical calculations. The inconsistencies between theoretical and experimental outcomes could be ascribed to variables including fluctuations in binding energy, grain boundaries, and anisotropic behavior. The integration of experimental validation and theoretical modeling effectively closes the disparity that exists between theoretical predictions and empirical observations, further strengthening the dependability of our results.

The present work additionally investigates the impact of sound wave velocity directionality on $CuSbSe_2$ thin films, uncovering intricate details related to the elastic characteristics of the material. The power flow angle, enhancement factor, group wave velocity, and phase wave velocity analyses all help in furthering our understanding of the anisotropic characteristics exhibited by sound waves within $CuSbSe_2$ thin films.

The integration of theoretical and experimental methodologies in this study not only enhance our comprehension of the mechanical characteristics of $CuSbSe_2$ thin films, but also establish a strong correlation between theoretical forecasts and empirical results. The amalgamation of experimental methods and computational simulations makes a substantial scholarly contribution to the domain

of material science, facilitating additional investigations and practical implementations of $CuSbSe_2$ thin films across diverse technology sectors.

Acknowledgements

This work was supported by Turkish Scientific and Research Council (TUBITAK) under Grant no 120F286. The numerical calculations reported in this paper were performed at TUBITAK ULAKBIM, High Performance and Grid Computing Center (TRUBA resources) and Istanbul Technical University National Center for High Performance Computing (ITU-UHEM).

References

[1] Adeyinka A M, Mbelu O V., Adediji Y B and Yahya D I 2023 A Review of Current Trends in Thin Film Solar Cell Technologies *International Journal of Energy and Power Engineering* **17** 1–10

[2] Dambhare M V., Butey B and Moharil S V. 2021 Solar photovoltaic technology: A review of different types of solar cells and its future trends *J Phys Conf Ser* **1913** 012053

[3] Sharma S, Jain K K and Sharma A 2015 Solar Cells: In Research and Applications—A Review *Materials Sciences and Applications* **06** 1145–55

[4] Green M A 2007 Thin-film solar cells: Review of materials, technologies and commercial status *J Mater Sci-Mater El* **18** 15–9

[5] Mittiga A, Salza E, Sarto F, Tucci M and Vasanthi R 2006 Heterojunction solar cell with 2% efficiency based on a Cu2O substrate *Appl Phys Lett* **88**

[6] Wu Y, Wadia C, Ma W, Sadtler B and Alivisatos A P 2008 Synthesis and photovoltaic application of copper(1) sulfide nanocrystals *Nano Lett* **8** 2345–50

[7] Puthussery J, Seefeld S, Berry N, Gibbs M and Law M 2011 Colloidal iron pyrite (FeS2) nanocrystal inks for thin-film photovoltaics *J Am Chem Soc* **133** 716–9

[8] Berry N, Cheng M, Perkins C L, Limpinsel M, Hemminger J C and Law M 2012 Atmospheric-Pressure Chemical Vapor Deposition of Iron Pyrite Thin Films *Adv Energy Mater* **2** 1124–35

[9] Sinsermsuksakul P, Hartman K, Bok Kim S, Heo J, Sun L, Hejin Park H, Chakraborty R, Buonassisi T and Gordon R G 2013 Enhancing the efficiency of SnS solar cells via band-offset engineering with a zinc oxysulfide buffer layer *Appl Phys Lett* **102**

[10] Li Y, Wei H, Cui C, Wang X, Shao Z, Pang S and Cui G 2023 CZTSSe solar cells: insights into interface engineering *J Mater Chem A Mater* **11** 4836–49

[11] Dhawale D S, Ali A and Lokhande A C 2019 Impact of various dopant elements on the properties of kesterite compounds for solar cell applications: a status review *Sustain Energy Fuels* **3** 1365–83

[12] Mitzi D B, Gunawan O, Todorov T K, Wang K and Guha S 2011 The path towards a high-performance solution-processed kesterite solar cell *Sol Energ Mat Sol C* **95** 1421–36

[13] Wang W, Winkler M T, Gunawan O, Gokmen T, Todorov T K, Zhu Y and Mitzi D B 2014 Device Characteristics of CZTSSe Thin-Film Solar Cells with 12.6% Efficiency *Adv Energy Mater* **4** 1301465

[14] Xue D-J, Yang B, Yuan Z-K, Wang G, Liu X, Zhou Y, Hu L, Pan D, Chen S, Tang J, Xue D, Yang B, Liu X, Zhou Y, Hu L, Tang J, Yuan Z, Wang G, Pan D and Chen S 2015 CuSbSe2 as a Potential Photovoltaic Absorber Material: Studies from Theory to Experiment *Adv Energy Mater* **5** 1501203
[15] Welch A W, Baranowski L L, Zawadzki P, Lany S, Wolden C A and Zakutayev A 2015 CuSbSe2 photovoltaic devices with 3% efficiency *Appl Phys Express* **8** 082301
[16] Yu L, Kokenyesi R S, Keszler D A, Zunger A, Yu L, Zunger A, Kokenyesi R S and Keszler A 2013 Inverse Design of High Absorption Thin-Film Photovoltaic Materials *Adv Energy Mater* **3** 43–8
[17] Tiwari K J, Vinod V, Subrahmanyam A and Malar P 2017 Growth and characterization of chalcostibite CuSbSe2 thin films for photovoltaic application *Appl Surf Sci* **418** 216–24
[18] Rampino S, Pattini F, Bronzoni M, Mazzer M, Sidoli M, Spaggiari G and Gilioli E 2018 CuSbSe2 thin film solar cells with ~4% conversion efficiency grown by low-temperature pulsed electron deposition *Sol Energ Mat Sol C* **185** 86–96
[19] Surucu O, Isik M, Terlemezoglu M, Bektas T, Gasanly N M and Parlak M 2022 Temperature effects on optical characteristics of thermally evaporated CuSbSe2 thin films for solar cell applications *Opt Mater (Amst)* **133** 113047
[20] Gerthoffer A, Poulain C, Roux F, Emieux F, Grenet L and Perraud S 2017 CIGS solar cells on ultra-thin glass substrates: Determination of mechanical properties by nanoindentation and application to bending-induced strain calculation *Sol Energ Mat Sol C* **166** 254–61
[21] Lin Y-C, Peng X-Y, Wang L-C, Lin Y-L, Wu C-H and Liang S-C 2014 Residual stress in CIGS thin film solar cells on polyimide: simulation and experiments *J Mater Sci-Mater El* **25** 461–5
[22] Gleskova H, Cheng I C, Wagner S, Sturm J C and Suo Z 2006 Mechanics of thin-film transistors and solar cells on flexible substrates *Sol Energy* **80** 687–93
[23] Luo S, Lee J H, Liu C W, Shieh J M, Shen C H, Wu T T, Jang D and Greer J R 2014 Strength, stiffness, and microstructure of Cu(In,Ga)Se2 thin films deposited via sputtering and co-evaporation *Appl Phys Lett* **105**
[24] Hu Z, Aigouy L, Chen Z and Fournier D 2020 Thermal conductivity and diffusivity of triple-cation perovskite halide materials for solar cells *J Appl Phys* **127**
[25] Yue S Y, Zhang X, Qin G, Yang J and Hu M 2016 Insight into the collective vibrational modes driving ultralow thermal conductivity of perovskite solar cells *Phys Rev B* **94** 115427
[26] Kresse G and Furthmüller J 1996 Efficiency of ab-initio total energy calculations for metals and semiconductors using a plane-wave basis set *Comput Mater Sci* **6** 15–50
[27] Kresse G and Furthmüller J 1996 Efficient iterative schemes for *ab initio* total-energy calculations using a plane-wave basis set *Phys Rev B* **54** 11169
[28] Perdew J P, Burke K and Ernzerhof M 1996 Generalized Gradient Approximation Made Simple *Phys Rev Lett* **77** 3865
[29] Kresse G and Joubert D 1999 From ultrasoft pseudopotentials to the projector augmented-wave method *Phys Rev B* **59** 1758
[30] Blöchl P E 1994 Projector augmented-wave method *Phys Rev B* **50** 17953
[31] Pack J D and Monkhorst H J 1977 "Special points for Brillouin-zone integrations"—a reply *Phys Rev B* **16** 1748

[32] Hoover W G, Ladd A J C and Moran B 1982 High-Strain-Rate Plastic Flow Studied via Nonequilibrium Molecular Dynamics *Phys Rev Lett* **48** 1818
[33] Evans D J 1983 Computer ‘“experiment”’ for nonlinear thermodynamics of Couette flow *J Chem Phys* **78** 3297–302
[34] Lemons D S and Gythiel A 1997 Paul Langevin’s 1908 paper “On the Theory of Brownian Motion” [“Sur la théorie du mouvement brownien,” C. R. Acad. Sci. (Paris) 146, 530–533 (1908)] *Am J Phys* **65** 1079–81
[35] Jinnouchi R, Karsai F, Verdi C, Asahi R and Kresse G 2020 Descriptors representing two-and three-body atomic distributions and their effects on the accuracy of machine-learned inter-atomic potentials *J Chem Phys* **152**
[36] Jinnouchi R, Karsai F and Kresse G 2019 On-the-fly machine learning force field generation: Application to melting points *Phys Rev B* **100** 014105
[37] Behler J and Parrinello M 2007 Generalized neural-network representation of high-dimensional potential-energy surfaces *Phys Rev Lett* **98** 146401
[38] Tang W, Sanville E and Henkelman G 2009 A grid-based Bader analysis algorithm without lattice bias *J Phys-Condens Mat* **21** 084204
[39] R. F. W. Bader 1990 Atoms in Molecules: A Quantum Theory, Oxford University Press 438
[40] Momma K and Izumi F 2011 VESTA 3 for three-dimensional visualization of crystal, volumetric and morphology data *J Appl Crystallogr* **44** 1272-1276
[41] Le Page Y and Saxe P 2002 Symmetry-general least-squares extraction of elastic data for strained materials from *ab initio* calculations of stress *Phys Rev B* **65** 104104
[42] Lyakhov A O and Oganov A R 2011 Evolutionary search for superhard materials: Methodology and applications to forms of carbon and TiO2 *Phys Rev B Condens Matter Mater Phys* **84** 092103
[43] Gaillac R, Pullumbi P and Coudert F X 2016 ELATE: an open-source online application for analysis and visualization of elastic tensors *J Phys-Condens Mat* **28** 275201
[44] Jaeken J W and Cottenier S 2016 Solving the Christoffel equation: Phase and group velocities *Comput Phys Commun* **207** 445–51
[45] Fedorov F I 1968 General Equations of the Theory of Elasticity *Theory of Elastic Waves in Crystals* 1–33
[46] Welch A W, Baranowski L L, Zawadzki P, Lany S, Wolden C A and Zakutayev A 2015 CuSbSe2 photovoltaic devices with 3% efficiency *Appl Phys Express* **8** 082301
[47] Surucu O, Isik M, Terlemezoglu M, Bektas T, Gasanly N M and Parlak M 2022 Temperature effects on optical characteristics of thermally evaporated CuSbSe2 thin films for solar cell applications *Opt Mater (Amst)* **133** 113047
[48] Surucu G, Bal E, Gencer A, Parlak M and Surucu O 2024 Performance analysis of CuSbSe2 thin-film solar cells with Cd-free window layers *Mater Lett* **363** 136296
[49] Temple D J, Kehoe A B, Allen J P, Watson G W and Scanlon D O 2012 Geometry, electronic structure, and bonding in CuMCh 2(M = Sb, Bi; Ch = S, Se): Alternative solar cell absorber materials? *J Phys Chem C* **116** 7334–40
[50] Baker J, Kumar R S, Sneed D, Connolly A, Zhang Y, Velisavljevic N, Paladugu J, Pravica M, Chen C, Cornelius A and Zhao Y 2015 Pressure induced structural transitions in CuSbS2 and CuSbSe2 thermoelectric compounds *J Alloys Compd* **643** 186–94

[51] Merino J M, Díaz-Moreno S, Subías G and León M 2005 A comparative study of Cu–Se and In–Se bond length distributions in CuInSe2 with related In-rich compounds *Thin Solid Films* **480–481** 295–300
[52] Deringer V L, Stoffel R P, Wuttig M and Dronskowski R 2015 Vibrational properties and bonding nature of Sb2Se3 and their implications for chalcogenide materials *Chem Sci* **6** 5255–62
[53] Born M 1940 On the stability of crystal lattices. I *Math Proc Cambridge* **36** 160–72
[54] Prudhvi Raju N and Thangavel R 2020 Theoretical investigation of spin–orbit coupling on structural, electronic and optical properties for CuAB2 (A = Sb, Bi; B = S, Se) compounds using Tran–Blaha-modified Becke–Johnson method: A first-principles approach *J Alloys Compd* **830** 154621
[55] Surucu G 2018 Investigation of structural, electronic, anisotropic elastic, and lattice dynamical properties of MAX phases borides: An Ab-initio study on hypothetical M2AB (M = Ti, Zr, Hf; A = Al, Ga, In) compounds *Mater Chem Phys* **203** 106–17
[56] Isik M, Surucu G, Gencer A and Gasanly N M 2021 Electronic, optical and thermodynamic characteristics of Bi12SiO20 sillenite: First principle calculations *Mater Chem Phys* **267** 124711
[57] Clarke D R and Levi C G 2003 Materials Design for the Next Generation Thermal Barrier Coatings *Ann Rev Mater Res* **33** 383–417
[58] Cahill D G, Watson S K and Pohl R O 1992 Lower limit to the thermal conductivity of disordered crystals *Phys Rev B* **46** 6131
[59] Ledbetter H and Migliori A 2006 A general elastic-anisotropy measure *J Appl Phys* **100** 63516
[60] Li X and Bhushan B 2002 A review of nanoindentation continuous stiffness measurement technique and its applications *Mater Charact* **48** 11–36
[61] Oliver W C and Pharr G M 1992 An improved technique for determining hardness and elastic modulus using load and displacement sensing indentation experiments *J Mater Res* **7** 1564–83
[62] Zhang W, Song H Z, Zhang Z, Luo H, Jiang Y, Xie X, Yao C, Yuan L, Deng J, Hu W, Chen Q, Huang H, Dai Q, Hao X and Liu Q 2019 Determination of mechanical behaviors of Ho3+:BaY2F8 single crystals by nanoindentation *Ceram Int* **45** 21751–8
[63] Şahin O, Uzun O, Kölemen U and Uçar N 2008 Analysis of ISE in dynamic hardness measurements of β-Sn single crystals using a depth-sensing indentation technique *Mater Charact* **59** 729–36
[64] Grishin A M 2020 Hardness, Young's Modulus and Elastic Recovery in Magnetron Sputtered Amorphous AlMgB14 Films *Crystals* **10** 823
[65] Ma Y, Huang X, Hang W, Liu M, Song Y, Yuan J and Zhang T 2020 Nanoindentation size effect on stochastic behavior of incipient plasticity in a LiTaO3 single crystal *Eng Fract Mech* **226** 106877
[66] Gong J, Miao H, Peng Z and Qi L 2003 Effect of peak load on the determination of hardness and Young's modulus of hot-pressed Si3N4 by nanoindentation *Mat Sci Eng A-Struct* **354** 140–5
[67] Lamuta C, Campi D, Cupolillo A, Aliev Z S, Babanly M B, Chulkov E V., Politano A and Pagnotta L 2016 Mechanical properties of Bi2Te3 topological insulator investigated by density functional theory and nanoindentation *Scr Mater* **121** 50–5

[68] Aouadi S M 2006 Structural and mechanical properties of TaZrN films: Experimental and ab initio studies *J Appl Phys* **99**
[69] Chen Q, Gao F, Csanádi T, Xu J, Fu M, Wang M and Dusza J 2018 Investigation of anisotropic mechanical properties of textured KSr2Nb5O15 ceramics via ab-initio calculation and nanoindentation *J Am Ceram Soc* **101** 5138–50